molecules

MDPI

Article

Numerical Investigation of a Cross-Wavelength Hierarchical Metasurface for Integrated THz Sensing and SERS Enhancement

Meilan Ge [1,*] and Yu Cao [2]

[1] Department of Neurosurgery, Tangdu Hospital, The Fourth Military Medical University, Xi'an 710038, China
[2] College of Chemistry and Chemical Engineering, Xiamen University, Xiamen 361005, China; yucao_xmu@163.com
* Correspondence: meilange@tju.edu.cn

Abstract

A cross-wavelength hierarchical metasurface sensor (CHMS) integrating terahertz (THz) sensing and surface-enhanced Raman scattering (SERS) enhancement is proposed and numerically investigated. The structure combines microscale Au resonators with truncated-pyramidal Au nanostructures to support THz resonances and localized optical near fields, respectively. Four THz resonances are obtained, among which the 1.70 THz mode exhibits the strongest refractive-index response with a sensitivity of 133.4 GHz/RIU. In the optical regime, the dominant gap-field enhancement occurs near 621.2 nm, and 633 nm is adopted as a representative Raman excitation wavelength. The SERS nanoarray only weakly perturbs the THz response, while the optical simulations indicate that the localized near-field enhancement is primarily associated with the Au nanostructures and their nanogap coupling, with the local supporting environment influencing the optical response. Dimensional and positional-deviation analyses further show that the THz resonance frequencies remain relatively stable within the investigated ranges, while the resonance depths and localized SERS fields are more sensitive to misalignment. These results provide guidance for the design and fabrication of integrated cross-wavelength THz–SERS metasurfaces.

Keywords: cross-wavelength metasurface; terahertz sensing; surface-enhanced Raman scattering; refractive-index sensing; plasmonic nanostructures; fabrication tolerance

1. Introduction

Terahertz (THz) spectroscopy and Raman spectroscopy are two complementary spectroscopic techniques for probing the structural and physicochemical properties of materials, enabling label-free and nondestructive characterization [1,2]. THz spectroscopy is particularly sensitive to low-frequency collective motions, intermolecular interactions, rotational dynamics, and dielectric responses [3]. Raman spectroscopy, in contrast, provides molecule-specific vibrational fingerprints associated with chemical bonds and molecular structures [4,5]. Owing to their distinct spectral ranges and interaction mechanisms [6,7], the combination of THz and Raman spectroscopy can provide complementary information across different length and frequency scales, offering a promising route toward more comprehensive material and biomolecular characterization.

Despite this complementarity, the implementation of THz–Raman dual-modal sensing remains limited by the relatively weak light–matter interaction in both spectral regimes. In the THz range, the large wavelength compared with molecular dimensions generally results in limited sensitivity to small dielectric perturbations. Metasurfaces composed of

Check for updates

Academic Editors: Mauricio Alcolea Palafox and Przemyslaw Niedzielski

Received: 20 October 2026
Revised: 15 November 2026
Accepted: 24 November 2026
Published: 26 November 2026

Copyright: © 2026 by the authors. Licensee MDPI, Basel, Switzerland. This article is an open access article distributed under the terms and conditions of the Creative Commons Attribution (CC BY) license.

engineered subwavelength resonators provide an effective means of enhancing THz sensing by concentrating electromagnetic fields and increasing the spectral response to changes in the surrounding dielectric environment [8–10]. In Raman spectroscopy, the intrinsically small scattering cross section leads to weak signals, particularly for trace analytes [11]. This limitation can be substantially alleviated by surface-enhanced Raman scattering (SERS), in which plasmonic nanostructures generate strongly enhanced local electromagnetic fields and thereby amplify Raman signals [12]. Therefore, integrating THz resonant structures with SERS-active nanostructures offers a potential route toward cross-wavelength sensing within a single platform.

Recent studies have demonstrated substantial progress in high-performance THz sensing and integrated THz–SERS sensors. Zhang et al. developed a PVDF-based THz surface plasmon resonance (SPR) fiber sensor and evaluated its dimensional fabrication tolerance [13]. Xue et al. proposed a MoS_2-based dual-channel THz SPR fiber sensor [14], while Agarwal et al. reported an all-dielectric THz metasurface sensor exhibiting high sensitivity, quality factors, and figures of merit [15]. Meanwhile, cross-wavelength THz-SERS sensing has also been demonstrated. Wang et al. developed a cross-wavelength hierarchical metamaterial combining microscale THz resonators with nanoscale Ag nanocube structures. The sensor enabled simultaneous THz and SERS detection of bacteria and their metabolites [6]. More recently, Jin et al. reported a THz/SERS dual-mode immunoassay based on a polarization-independent metamaterial integrated with a Au nanoparticle-based SERS nanoprobe for the detection of multiple tumor markers [7]. These studies demonstrate the potential of both high-performance THz sensing and integrated THz–SERS sensing [12]. However, the electromagnetic responses of hierarchical THz–SERS sensors depend on their specific structural configuration. In particular, the effects of fabrication-induced dimensional deviations, interlayer misalignment of THz resonators, and local positional deviations of SERS nanostructures on the corresponding electromagnetic responses warrant further investigation.

In this work, we numerically investigate a cross-wavelength hierarchical metasurface sensor (CHMS) integrating THz sensing and SERS enhancement within a multilayer architecture. The structure consists of microscale patterned Au resonators for the THz response and periodically arranged truncated square-pyramidal Au nanostructures for optical near-field enhancement. The THz characteristics are investigated through the transmission response, refractive-index sensing behavior, electric field distributions, and surface current distributions, while the optical response and localized SERS-related field enhancement are analyzed. Moreover, we investigate the influence of introducing the Au nanoarray on the THz response and compare the optical responses of Au-supported and Si-supported nanoarrays. Furthermore, the effects of dimensional deviations and positional misalignment are systematically evaluated to assess the fabrication tolerance of the proposed structure. This study provides numerical insights into the electromagnetic characteristics and their sensitivity to structural deviations of the CHMS and offers guidance for the design of integrated cross-wavelength THz–SERS sensors.

2. Results and Discussion

2.1. Structural Configuration of the CHMS

The schematic illustration of the proposed cross-wavelength hierarchical metasurface sensor (CHMS) is presented in Figure 1. The proposed CHMS integrates both THz and SERS sensing functionalities within a single multilayer architecture. Figure 1a shows the overall configuration of the CHMS together with the incident THz wave, optical excitation, THz signal, and SERS signal. In the THz simulations, the incident wave propagates normally along the -z direction, with the electric field polarized along the x direction. As illustrated

in Figure 1b, the CHMS consists of a silicon (Si) substrate, two polyimide (PI) dielectric layers, and two patterned Au metallic layers. The two metallic layers are separated by a PI dielectric spacer, forming a vertically integrated hierarchical architecture for the THz and optical responses. Figure 1c,d show the top views of the unit cells of the two Au metasurface layers. The upper Au layer consists of a periodic array of square patches with a side length b and a period P, whereas the lower Au layer consists of a periodic array of square-ring resonators characterized by the geometric parameters d, w, and P. The square-ring resonator primarily provides the microscale electromagnetic response in the THz frequency range.

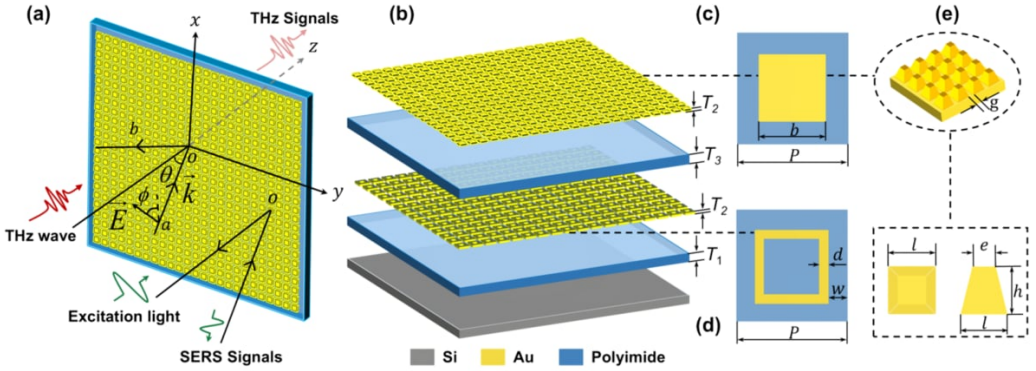

Figure 1. Schematic illustration of the proposed cross-wavelength hierarchical metasurface sensor (CHMS). (**a**) Overall configuration of the CHMS, showing the incident THz wave, excitation light, THz signal, and SERS signal. The THz wave is normally incident along the -z direction with the electric field polarized along the x direction. (**b**) Exploded view of the multilayer architecture, consisting of a Si substrate, two polyimide (PI) dielectric layers, and two patterned Au layers. (**c**) Top view of the upper Au metasurface unit cell, consisting of a periodic square patch with a side length b and period P. (**d**) Top view of the lower Au metasurface unit cell, consisting of square-ring resonators characterized by the geometric parameters d and w (**e**) Enlarged schematic of the truncated-pyramidal Au nanostructures, showing their characteristic dimensions and the nanoscale gap between adjacent nanostructures.

For the SERS response, the surface of the upper square Au patch is further decorated with a periodic array of truncated square-pyramidal Au nanostructures, as illustrated in Figure 1e. Each truncated pyramid has a base side length l and a height h, and the edge-to-edge gap between adjacent pyramids is g. The nanoscale gaps between neighboring pyramids provide strong localized optical-field enhancement for electromagnetic SERS enhancement.

2.2. THz Spectral Response and Refractive Index Sensing Performance

Figure 2 presents the response and refractive index sensing characteristics of the proposed CHMS. As illustrated in Figure 2a, a 10 μm-thick analyte layer was introduced on the metasurface to modify the local dielectric environment surrounding the resonant structure. The resulting dielectric perturbation alters the resonance condition and can therefore be detected through changes in the THz transmission spectrum. As shown in Figure 2b, the CHMS exhibits four distinct resonance dips at approximately 0.50, 1.18, 1.36, and 1.70 THz under normal incidence, respectively. These resonance features demonstrate the multi-band THz response of the hierarchical metasurface within the investigated frequency range. Figure 2c shows the transmittance spectra when the refractive index of the analyte layer is varied from 1.1 to 1.6. The resonances near 1.18, 1.36, and 1.70 THz exhibit clear red-shifts with increasing refractive index, whereas the resonance near 0.5 THz remains nearly unchanged. Among these modes, the resonance near 1.70 THz shows the largest spectral shift.

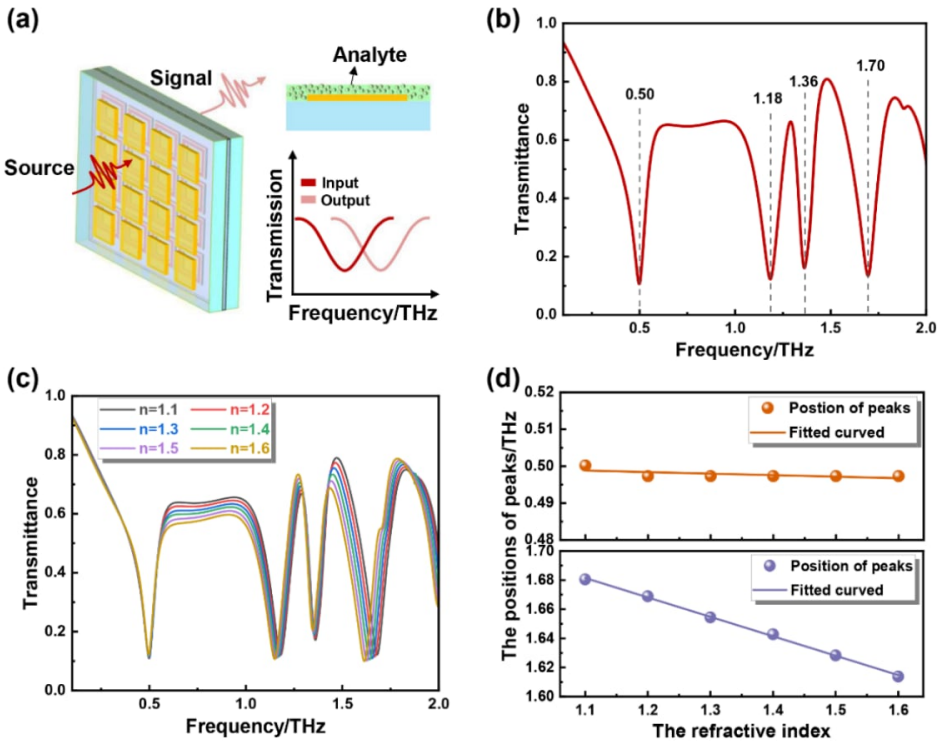

Figure 2. THz response and refractive index sensing characteristics of the proposed CHMS. (**a**) Schematic illustration of the THz sensing configuration with a 10 μm-thick analyte layer covering the metasurface. (**b**) Simulated THz transmittance spectrum under normal incidence. (**c**) Transmittance spectra for analyte refractive indices ranging from 1.1 to 1.6. (**d**) Extracted resonance frequencies and linear fitting results for the resonances near 0.50 THz (**top**) and 1.70 THz (**bottom**) as a function of the analyte refractive index.

The observed redshift results from the increased dielectric loading of the resonant structure as the refractive index of the surrounding medium increases. The different spectral responses of the four resonances indicate that the corresponding electromagnetic modes interact with the analyte region to different extents. To quantitatively compare the refractive-index responses, the resonance frequencies near 0.50 and 1.70 THz were extracted and plotted as functions of the analyte refractive index, as shown in Figure 2d. The 0.50 THz resonance exhibits only a small frequency variation, whereas the 1.70 THz resonance shows a nearly linear redshift with increasing refractive index. The linear fitting result for the 1.70 THz mode gives a coefficient of determination of $R^2 = 0.9986$, indicating a stable correlation between the resonance frequency and the analyte refractive index within the investigated range.

The refractive index sensitivity S is defined as [16]:

$$S = \frac{\Delta f}{\Delta n}$$

where Δf is the resonance frequency shift and Δn is the corresponding change in refractive index.

For the resonance near 1.70 THz, $|(1.6138 - 1.6805)/(1.6 - 1.1)| = 0.1334$ THz/RIU, corresponding to 133.4 GHz/RIU.

The spectral characteristics of this sensing mode were further evaluated using the quality factor Q and figure of merit (FOM). The quality factor is defined as [17]:

$$Q = \frac{f_0}{FWHM}$$

where f_0 is the resonance frequency and FWHM is the full width at half maximum of the resonance. The corresponding Q factor of the 1.70 THz resonance is 1.70/0.129 = 13.18.

The FOM is given by [17]:

$$FOM = \frac{S}{FWHM}$$

The calculated *FOM* of the 1.70 THz resonance is 0.1334/0.129 = 1.03 RIU^{-1}. These parameters characterize the spectral sensitivity and linewidth of the 1.70 THz resonance and support its use as the primary refractive-index sensing mode of the proposed CHMS.

Compared with the all-dielectric THz sensor reported in [15], which achieved sensitivities of 1000 and 2000 GHz/RIU, Q factors of 920 and 685.53, and *FOM*s of 514.40 and 351.55 RIU^{-1}, respectively, the proposed CHMS does not exhibit superior THz sensing metrics. However, the main contribution of this work lies in the numerical investigation of a hierarchical THz–SERS architecture, particularly the influence of structural deviations at both microscale and nanoscale levels. Because the sensor configurations and evaluation conditions differ, these performance metrics should not be interpreted as a direct comparison under identical conditions.

To further clarify the different refractive-index responses of the resonances, the corresponding electric field and surface current distributions at 0.50 and 1.70 THz are analyzed in Figure 3. The corresponding distributions for all four resonances at 0.50, 1.18, 1.36, and 1.70 THz are provided in Figures S1 and S2. At 0.50 THz, the electric field is mainly concentrated near the metallic edges, while the surface current is predominantly distributed around the lower square-ring resonator. Because the electric field of the 0.50 THz mode is mainly confined around the lower resonator, its spatial overlap with the analyte region is limited, resulting in a weak refractive-index response. In contrast, the 1.70 THz resonance exhibits a different electric field distribution and surface current pattern, indicating a distinct electromagnetic mode. Compared with the 0.50 THz resonance, the 1.70 THz mode shows greater spatial overlap with the analyte region. This results in a stronger refractive-index response. This enhanced spatial overlap is consistent with the larger refractive-index-dependent frequency shift observed in Figure 2c. Therefore, the sensing performance of the CHMS is governed not only by the magnitude of the local electromagnetic field, but also by its spatial overlap with the analyte region.

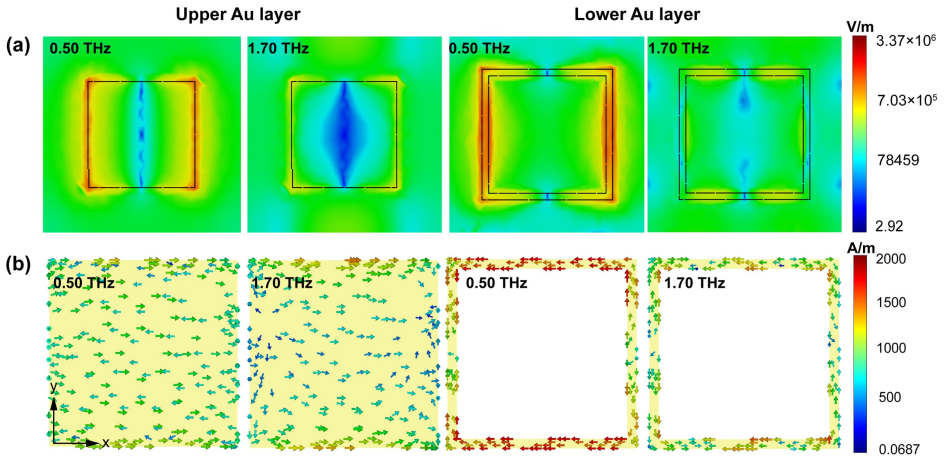

Figure 3. Electric field and surface current distributions of the proposed CHMS at 0.50 and 1.70 THz. (**a**) Electric field distributions in representative planes corresponding to the upper and lower Au layers. (**b**) Corresponding surface current distributions on the upper and lower Au layers. The left and right columns in each correspond to 0.50 and 1.70 THz, respectively.

2.3. Optical Response and SERS Electromagnetic Enhancement

Figure 4 presents the optical response and localized electromagnetic-field characteristics of the proposed CHMS. Figure 4a shows the SERS configuration based on the periodic truncated-pyramidal Au nanoarray. The calculated absorption spectrum is shown in Figure 4b, where a distinct spectral feature appears at approximately 610.5 nm. To further evaluate the localized near-field response, the maximum electric field intensity enhancement in the gap plane, max $|E|^2/|E_0|^2$, was extracted as a function of wavelength, as shown in Figure 4c. The strongest near-field enhancement occurs at approximately 621.2 nm, together with weaker features near 577.7, 730.2, and 805.5 nm. It is worth noting that the wavelength of the maximum near-field enhancement does not exactly coincide with the absorption feature. This difference arises because the absorption spectrum represents the overall electromagnetic energy dissipation of the structure, whereas max $|E|^2/|E_0|^2$ reflects the strongest localized response within the nanoscale gap. Therefore, the far-field absorption response and the local near-field enhancement are not necessarily maximized at the same wavelength.

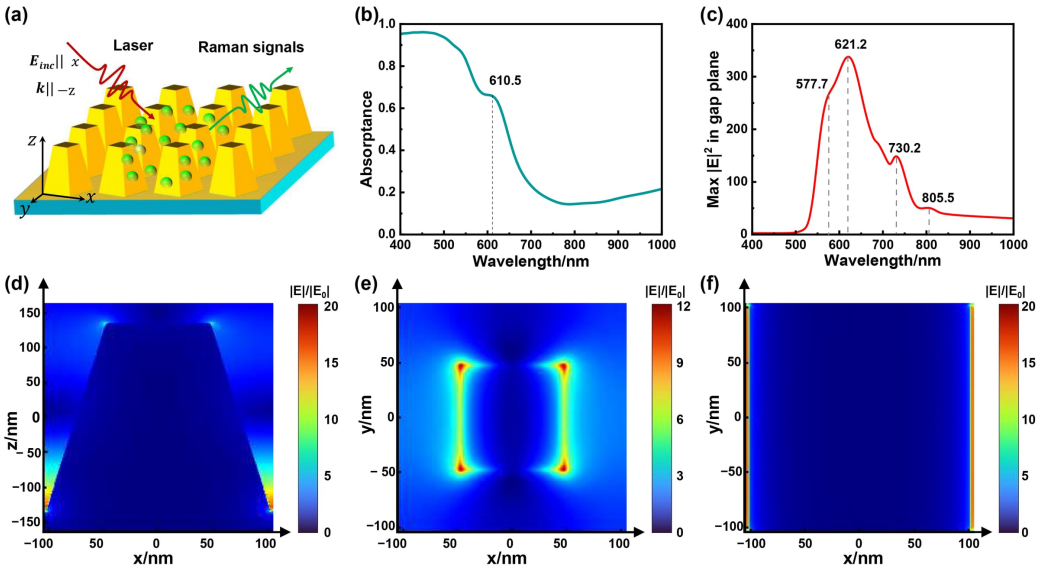

Figure 4. Optical response and localized electromagnetic-field characteristics of the proposed CHMS. (**a**) Schematic illustration of the periodic truncated-pyramidal Au nanoarray for SERS. The excitation light is normally incident along the −z direction, with its electric field polarized along the x direction. (**b**) Calculated absorption spectrum. (**c**) Maximum gap-plane electric field intensity enhancement, max $|E|_2/|E_0|^2$, as a function of wavelength. (**d**–**f**) Normalized electric field magnitude, $|E|/|E_0|$, at 633 nm in the central *x*–*z* plane, the upper *x*–*y* plane located 2 nm above the pyramid top surface, and the gap *x*–*y* plane located 5 nm above the pyramid bottom, respectively.

Although the strongest near-field enhancement occurs near 621.2 nm, 633 nm was selected as the representative excitation wavelength for the subsequent SERS analysis. This wavelength lies close to the dominant near-field resonance and is also commonly used for Raman excitation [18]. Figure 4d–f shows the normalized electric field magnitude, $|E|/|E_0|$, at 633 nm in the central *x*-*z* plane, the upper *x*-*y* plane located 2 nm above the pyramid top surface, and the gap *x*-*y* plane located 5 nm above the pyramid bottom, respectively. In the central *x*–*z* plane, the enhanced field is mainly localized near the lower edges of the truncated pyramid. In the upper *x*–*y* plane, the field enhancement is mainly concentrated around the lateral edges and four corners of the nanostructure. In contrast, the strongest localization is observed in the gap plane, where intense hotspots predominantly appear near the left and right boundaries of the unit cell. This difference can be attributed to the combined effects of the truncated-pyramidal geometry and the x-polarized excitation. Owing to the larger

lateral dimensions near the pyramid bottom, the gaps between adjacent nanostructures become narrower. Under x-polarized excitation, stronger plasmonic coupling occurs across the interparticle gaps along the polarization direction, resulting in pronounced field enhancement at the left and right boundaries. Such nanogap-localized field enhancement is consistent with previous studies of plasmonic SERS hotspots [19]. Owing to the periodic boundary conditions, these boundary-localized hotspots correspond to the nanoscale gaps between neighboring truncated-pyramidal Au nanostructures rather than numerical boundary artifacts. This result indicates that polarization-dependent interparticle gap coupling plays a major role in the localized electromagnetic enhancement.

The field distributions at 621 nm, near the 621.2 nm enhancement maximum, and at 633 nm are further compared in Figure S3. Similar hotspot locations and overall field patterns are observed at the two wavelengths, confirming that 633 nm preserves the characteristic spatial distribution of the dominant near-field resonance. In addition, the gap-plane field distributions at 532, 633, and 785 nm are compared in Figure S4 [18,20]. Although the enhancement magnitude varies with wavelength, the hotspots remain localized at similar geometrical positions. These results support the use of 633 nm as the representative excitation wavelength in the subsequent SERS analyses.

To further quantify the electromagnetic contribution to SERS, the $|E|^4$ approximation described in Section 3.1.2 was applied to the simulated electric field intensity enhancement at 633 nm. The maximum gap-plane electric field intensity enhancement was approximately 3.21×10^2, corresponding to an estimated maximum local electromagnetic SERS enhancement of approximately 1.03×10^5. This estimate assumes comparable local field enhancements at the excitation and Raman-scattered wavelengths. Therefore, the calculated value represents a hotspot-based electromagnetic enhancement estimate rather than an experimentally measured Raman enhancement factor, as the Raman-scattered wavelength dependence, molecular adsorption, and chemical enhancement effects were not explicitly considered.

2.4. Mutual Influence Between the THz and SERS Components

To evaluate the influence of the SERS nanostructure array on the THz response, the transmittance spectra of the CHMS with and without the Au nanoarray were compared, as shown in Figure 5a,b. The four resonance dips near 0.50, 1.18, 1.36, and 1.70 THz are preserved after introducing the SERS nanostructures, with only minor changes in resonance frequency and resonance depth. This weak perturbation can be attributed to the large difference in characteristic dimensions between the nanoscale SERS structures and the THz resonant elements. At THz frequencies, the SERS nanostructures are deeply subwavelength and therefore introduce only a limited perturbation to the THz electromagnetic response. These results indicate that the SERS nanoarray has little influence on the main THz resonance characteristics of the CHMS.

Conversely, the influence of the local supporting environment on the SERS response was evaluated by comparing two configurations of the same Au nanoarray, as illustrated in Figure 5c. In the first configuration, the nanoarray was placed on a continuous Au-supporting layer, representing the local approximation of the upper Au square patch in the CHMS. In the reference configuration, the Au-supporting layer was replaced by a Si substrate, while the nanoarray geometry and excitation conditions were kept unchanged. The corresponding maximum gap-plane electric field intensity enhancement spectra are shown in Figure 5d. Compared with the Au-supported configuration, the Si-supported nanoarray exhibits a substantially different spectral response, with several weaker features appearing near 579.6, 689.4, 723.9, 805.0, and 984.6 nm. These differences reflect the influence of the local supporting interface on the plasmonic coupling between adjacent nanostructures.

Specifically, replacing the continuous Au support with Si changes the metallic and dielectric boundary conditions beneath the nanoarray, leading to a redistribution of the optical near-field response.

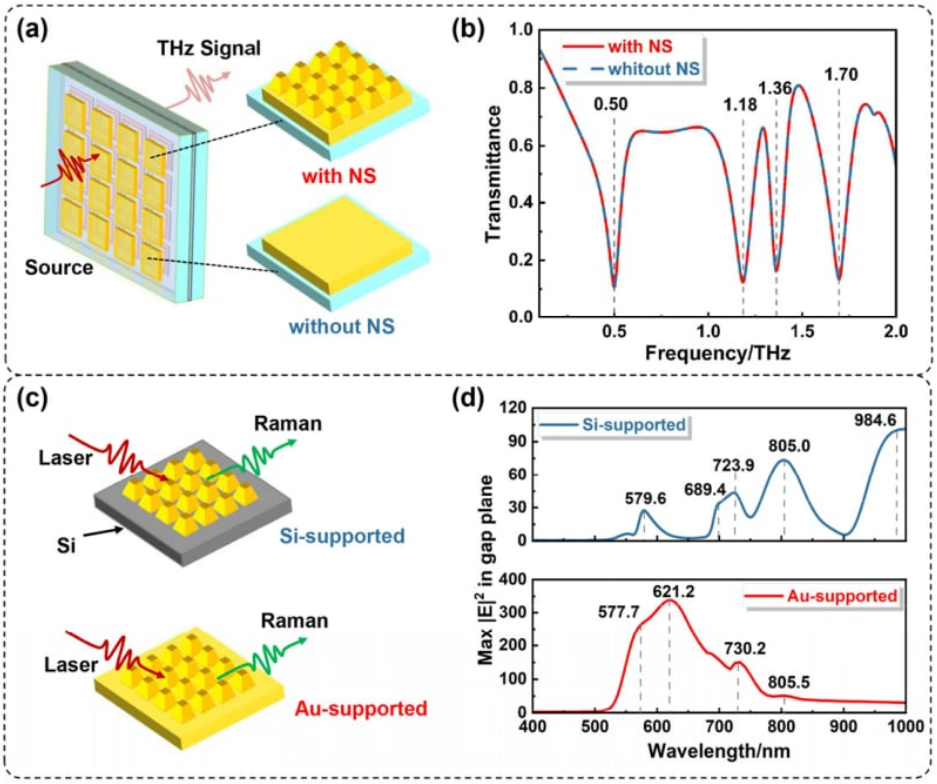

Figure 5. Mutual influence between the THz and SERS components and the influence of the local supporting environment on the optical response. (**a**) Schematic configurations of the THz structure with and without the SERS nanoarray. (**b**) Simulated THz transmittance spectra for the two configurations. (**c**) Schematic comparison of the SERS nanoarray directly supported by a Si substrate (Si-supported) and by a continuous Au layer (Au-supported). The latter represents a local approximation of the upper Au square patch in the CHMS. (**d**) Maximum gap-plane electric field intensity enhancement spectra of the Si-supported and Au-supported nanoarrays.

To further distinguish the contribution of the Au nanostructures from that of the supporting layer, an additional control simulation was performed using a bare Au layer without the truncated-pyramidal nanostructures. As shown in Figure S5, the maximum electric field intensity enhancement of the bare Au layer remains below 1 throughout the investigated wavelength range. At 633 nm, the maximum enhancement at the same monitoring plane is approximately 0.407 for the bare Au layer, compared with approximately 321 for the Au-supported nanoarray. This substantial difference indicates that the pronounced localized electromagnetic enhancement is primarily associated with the Au nanoarray and its nanogap coupling rather than the flat Au-supporting layer alone. Nevertheless, because the optical simulations employ a local Au-supported model rather than the complete multilayer CHMS, the contribution of the full THz resonator structure to the optical near-field response cannot be independently determined from these comparisons.

2.5. Fabrication Tolerance and Structural Robustness

To evaluate the influence of fabrication-induced dimensional deviations, representative geometrical parameters of the THz and SERS components were varied individually around their nominal values, while all other geometrical parameters and simulation settings were

kept unchanged. For the THz structure, the side length b of the upper Au square patch and the characteristic dimension d of the lower square-ring resonator were selected as representative parameters of the two metallic layers. As shown in Figure 6a, when b is varied by approximately ±5% around its nominal value, the relative frequency shifts in the four resonances remain within about ±3%, with the 0.50 THz mode showing the largest variation. In comparison, the resonance frequencies are less sensitive to changes in d; even for dimensional deviations of approximately ±10%, the frequency shifts remain within about ±1.2%, as shown in Figure 6b. These results indicate that the THz resonance frequencies remain relatively stable within the investigated dimensional variation ranges [21].

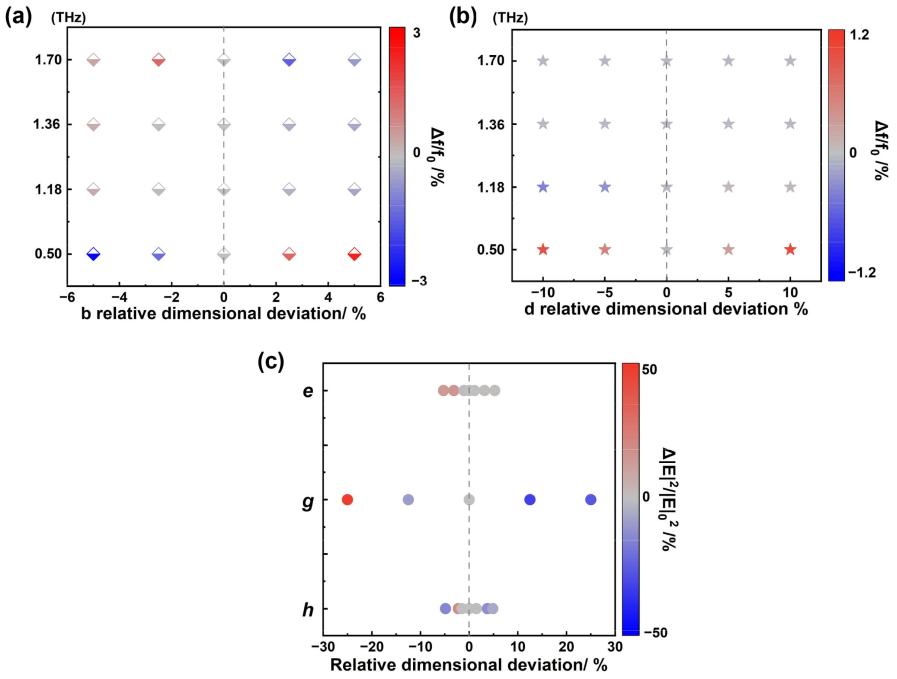

Figure 6. Influence of dimensional deviations on the THz and SERS responses of the proposed CHMS. (**a**,**b**) Relative resonance-frequency shifts in the four THz resonances as functions of the relative dimensional deviations in b and d, respectively. (**c**) Relative changes in the maximum gap-plane electric field intensity enhancement at 633 nm induced by variations in e, g, and h of the truncated-pyramid nanostructure. Different marker shapes are used for data distinction, and the color bar represents the THz value.

For the SERS nanostructure, the top size e, gap g, and height h were varied individually while the other parameters were kept unchanged. As shown in Figure 6c, the three parameters produce different changes in the maximum gap-plane electric field intensity enhancement at 633 nm. Among them, the gap produces the largest variation. Reducing the gap from 4 to 3 nm increases the maximum field enhancement by approximately 48.6%, whereas increasing the gap to 4.5 and 5 nm decreases it by approximately 32.3% and 26.9%, respectively. Variations in e and h generally produce smaller changes over the investigated ranges. These results indicate that, within the investigated variation ranges, the nanoscale gap has the strongest influence on the SERS near-field response [22]. It should be noted that the relative variation ranges of the three SERS parameters are different because of their different nominal dimensions, particularly the 4 nm gap. Therefore, the responses shown in Figure 6c are used to compare the effects of dimensional deviations within the investigated ranges rather than to define a normalized sensitivity to each geometrical parameter.

In addition to dimensional deviations, interlayer lateral misalignment may also occur during multilayer fabrication and affect the electromagnetic coupling between the THz resonators. To

evaluate this effect, the lower square-ring layer was kept fixed while only the upper square-patch Au layer was laterally displaced, as schematically shown in Figure 7a–c. All other geometrical parameters, material properties, and simulation settings were maintained unchanged. The upper layer was displaced along the x, y, and 45° directions with total displacement magnitudes D of 0, 2, 4, 6, and 8 μm, corresponding to relative displacements D/P of 0, 1.33, 2.67, 4.00, and 5.33%, respectively. For the 45° displacement, the in-plane components satisfy $d_x = d_y = D/\sqrt{2}$.

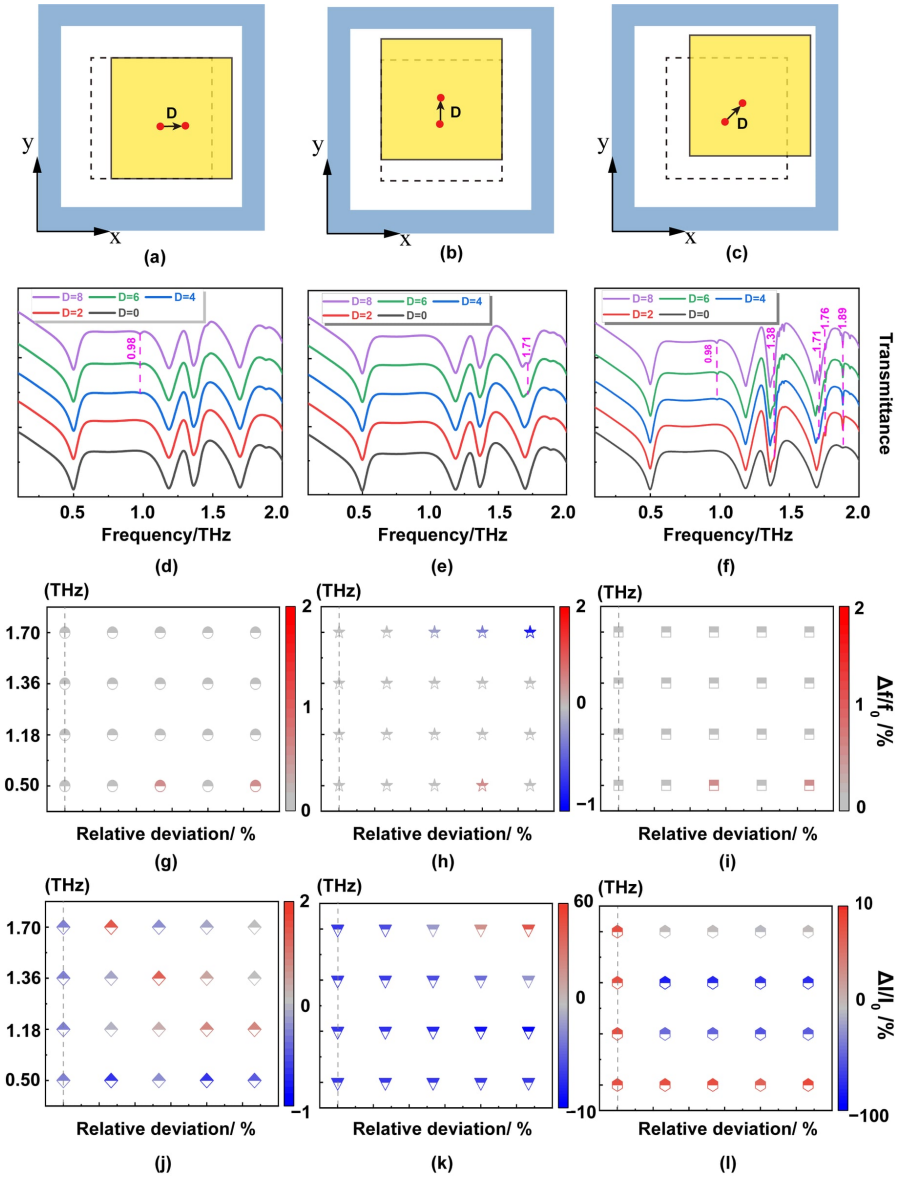

Figure 7. Effects of interlayer lateral misalignment on the THz response of the proposed CHMS. (**a**–**c**) Top-view schematic illustrations of the interlayer misalignment configurations along the x, y, and 45° directions, respectively. The blue square ring represents the fixed lower Au square-ring resonator, while the yellow square represents the displaced upper Au square patch. The dashed square indicates the initial aligned position of the upper Au patch, and D denotes the lateral displacement magnitude. (**d**–**f**) Simulated THz transmittance spectra under the corresponding displacement configurations, with displacement magnitudes D of 0, 2, 4, 6, and 8 μm, respectively. (**g**–**i**) Relative resonance-frequency shifts, $\Delta f/f_0$, of the four original THz resonances under the corresponding displacement configurations. (**j**–**l**) Relative variations in the resonance depth, $\Delta I/I_0$, for the four original resonances at approximately 0.50, 1.18, 1.36, and 1.70 THz. (**g**-**l**) Different marker shapes are used for data distinction, and the color bar represents the THz value.

As shown in Figure 7d–f, the four original resonances near 0.50, 1.18, 1.36, and 1.70 THz are retained over the investigated displacement range. The detailed displacement magnitudes and the corresponding relative changes in resonance frequency and resonance depth for the x, y, and 45° displacement directions are summarized in Table S1. As shown in Figure 7g–i, for displacements along the x and y directions, the resonance positions show only small variations, and the overall spectral profiles remain relatively stable. The relative frequency shifts in the original resonances are generally below 1–2% within the investigated range. In comparison, the 45° displacement produces more evident spectral restructuring, particularly in the high-frequency region, where additional spectral features appear at larger offsets.

The resonance-depth variations exhibit a stronger dependence on displacement direction and resonance mode, as shown in Figure 7j–l. For the x direction displacement, the resonance-depth changes in the four original modes remain small, generally within a few percent. The y-direction displacement has a stronger influence on the higher-frequency modes, with the resonance-depth variation in the 1.70 THz mode reaching approximately 52.9% at $D/P = 5.33\%$. The 45° displacement causes the largest redistribution of the spectral response: the resonance-depth changes in the 1.18 and 1.36 THz modes reach approximately 70–90%, while that of the 1.70 THz mode is about 40–50% over the investigated range. Overall, these results indicate that the THz resonance frequencies of the original THz modes are relatively stable under the investigated lateral misalignments, whereas their resonance depths and spectral profiles are more sensitive to interlayer positioning, particularly for diagonal displacement. This anisotropic response can be attributed to changes in the relative lateral alignment and electromagnetic coupling between the upper and lower resonators. A displacement along a single in-plane direction perturbs the interlayer coupling primarily along one axis, whereas the 45° displacement simultaneously modifies the coupling configuration along both the x and y directions. This combined perturbation leads to a stronger redistribution of the interlayer electromagnetic interaction, resulting in larger changes in resonance depth and spectral line shape. Notably, large changes in resonance depth may reduce spectral contrast and make resonance identification and frequency tracking more susceptible to measurement noise. Therefore, the relatively small resonance-frequency shifts should not be interpreted as overall robustness of the THz sensing performance, as substantial changes in resonance depth may compromise the precision and reliability of practical refractive-index measurements.

The influence of local positional deviations on the SERS near-field response was further investigated using a 3 × 3 supercell containing nine truncated-pyramidal Au nanostructures, as schematically illustrated in Figure 8a. The eight surrounding nanostructures were kept at their nominal lattice positions, while only the central nanostructure was laterally displaced. This configuration was used to represent a local placement error without translating the entire periodic nanoarray. The central nanostructure was displaced along the x, y, and 45° directions with total displacement magnitudes D of 0, 1, and 2 nm, corresponding to relative positional deviations D/P of approximately 0, 0.48, and 0.96%, respectively. For the 45° displacement, the in-plane components satisfy $d_x = d_y = D/\sqrt{2}$. A uniform mesh size of 1 nm was employed throughout the entire 3 × 3 supercell for all displacement configurations to ensure consistent numerical discretization while maintaining a feasible computational cost. All other geometrical parameters and simulation settings were kept unchanged. For a representative mesh-refinement analysis, the local mesh size around the central nanostructure was reduced to 0.75 nm for the nominal configuration and a 2 nm displacement along the x direction, while the surrounding region retained the 1 nm mesh. The mean electric field intensity enhancement was also evaluated within a fixed observation window (x = 95–115 nm, y = −40–40 nm).

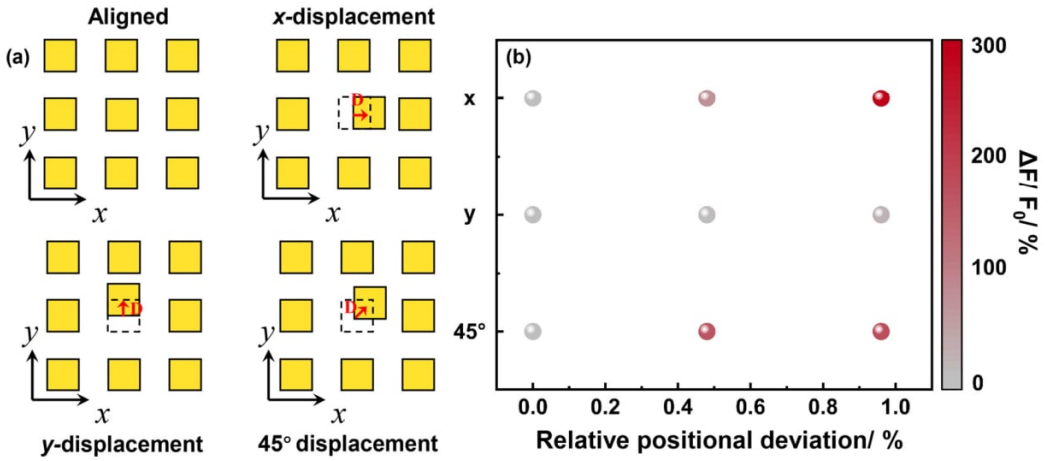

Figure 8. Influence of lateral positional deviations on the SERS nanostructures and the corresponding electric field intensity variations. (**a**) Top-view schematic illustrations of a 3 × 3 supercell showing the initial aligned configuration and the displacement of the central Au nanostructure along the x, y, and 45° directions. The eight surrounding nanostructures remain fixed. The dashed outlines indicate the initial position of the central nanostructure, and D denotes the displacement magnitude. The displacements are exaggerated for clarity. (**b**) Relative changes in the maximum gap-plane electric field intensity enhancement at 633 nm for different displacement directions and magnitudes ($D = 0$, 1, 2 nm). The relative change is defined as $\Delta F/F_0 = [F(\mathrm{D}) - F_0]/F_0$, where $F(\mathrm{D}) = \max(|E(\mathrm{D})|^2/|E_0|^2)$ and $F_0 = F(0)$.

As shown in Figure 8b, the maximum gap-plane electric field intensity enhancement at 633 nm exhibits direction-dependent variations under the original 1 nm mesh setting. For displacement along the x direction, the maximum relative field enhancement increases by approximately 75.5% and 289.7% at displacements of 1 and 2 nm, respectively. Displacement along the y direction produces much smaller changes of approximately 10.4% and 21.6%. For the 45° displacement, the corresponding increases are approximately 167.0% and 175.1%. The corresponding numerical values are summarized in Table S2. The directional dependence can be attributed to the redistribution of the nanoscale gaps around the displaced central nanostructure and the polarization-dependent plasmonic coupling. Under x-polarized excitation, displacement with an x-component modifies the interparticle separation along the polarization direction, narrowing the gap on one side of the central nanostructure and enlarging it on the opposite side. Such changes can alter the localized electromagnetic coupling and hotspot intensity.

To assess the numerical sensitivity of these results, the representative mesh-refinement analysis was conducted for the nominal configuration and the 2 nm x-direction displacement. As summarized in Table S3, the relative increase in the maximum local field-intensity enhancement changes from 289.7% to 97.2% when the local mesh size is refined from 1 to 0.75 nm. In comparison, the relative increase in the mean field-intensity enhancement within the fixed observation window changes from 55.3% to 68.1%. Both mesh settings therefore predict increased local field enhancement following the representative x-direction displacement, while the maximum enhancement values exhibit considerable numerical sensitivity. The actual field-sampling positions also differ slightly between the two mesh settings due to spatial discretization, which may contribute to the observed differences. These results support the qualitative enhancement trend for the representative displacement but indicate that numerical convergence of the maximum field enhancement has not yet been established. This limited refinement does not establish convergence of the mean field-enhancement values or of the results for other displacement configurations.

Overall, the SERS near-field enhancement is sensitive to local nanoscale positional deviations, particularly when the displacement contains a component parallel to the incident electric field polarization [23]. However, the quantitative variations in the maximum field enhancement reported in Figure 8b should be interpreted as mesh-dependent estimates rather than fully converged predictions.

3. Structural Design and Numerical Simulation

3.1. Numerical Methods

3.1.1. THz Numerical Simulation

The THz electromagnetic response of the proposed CHMS was investigated using three-dimensional full-wave electromagnetic simulations. The simulations were carried out using CST Studio Suite (2025, Dassault Systèmes, Vélizy-Villacoublay, France). The geometrical parameters used in the simulation are summarized in Table 1. To represent an infinite periodic metasurface, unit-cell boundary conditions were applied along the x and y directions, while open (add space) boundary conditions were employed along the z direction. The incident THz wave propagated normally along the –z direction, with the electric field polarized along the x direction. The excitation was implemented using a Floquet port. The simulated frequency range was set to 0.1–4.0 THz. The relative complex permittivity of polyimide was set to 3.5 + i 0.009 [24], while the relative permittivity of Si was taken as 11.7 [25]. The patterned Au layers were modeled as lossy conductors with an electrical conductivity of 4.09×10^7 S/m [26,27]. The THz transmittance was obtained from the frequency-dependent transmission S-parameter, $T = |S_{21}|^2$. Electric field distribution and surface current distribution at the characteristic resonance frequencies were further extracted to analyze the physical origin of the THz resonances.

Table 1. Geometrical parameters used in the THz and optical simulations.

THz-scale parameters/μm	T_1	T_2	T_3	P	b	d	w
	20	0.2	38	150	80	5	25
SERS-scale parameters/nm	g	l	e	h			
	4	205	95	268			

3.1.2. Optical and SERS Numerical Simulation

Three-dimensional finite-difference time-domain (FDTD) simulations were performed to investigate the optical response and electromagnetic field enhancement of the SERS nanostructure [28]. The optical field calculations were performed using Ansys Optics Launcher (2024 R1, Ansys, Canonsburg, PA, USA).The geometrical parameters used in the optical simulations were consistent with those defined in Figure 1 and summarized in Table 1. The frequency-dependent complex dielectric function of Au was taken from the optical constants reported by Johnson and Christy [29], and the surrounding medium was set to air. A linearly polarized plane wave was normally incident along the z direction, with the electric field polarized along the x direction. The wavelength range was set from 400 to 1000 nm to cover the relevant plasmonic response and representative Raman excitation wavelength. The incident electric field amplitude was set to $E_0 = 1$ V m^{-1}, which was used as the normalization reference for evaluating the local electric field enhancement.

Because the lateral dimension of the upper THz Au square patch is much larger than the period of the SERS nanoarray, the optical response was evaluated using a local unit-cell representation. For nanoarray regions sufficiently far from the patch edges, the upper Au square patch was locally approximated as a laterally continuous Au support beneath the nanostructure. Thus, the optical model represents the Au-supported SERS nanoarray rather than the complete multilayer CHMS architecture. Accordingly, a 1 × 1 SERS unit

cell with a period of 209 nm was used, with periodic boundary conditions applied along the x and y directions and perfectly matched layer (PML) boundary conditions along the z direction. For comparison, the continuous Au support was replaced by a Si substrate, while the nanoarray geometry, excitation conditions, and monitoring configuration were kept unchanged. Moreover, an additional reference configuration consisting of a bare Au-supporting layer without the truncated-pyramidal nanostructures was also simulated to distinguish the contribution of the nanostructured array from that of the flat Au layer. The excitation conditions, material parameters, and monitoring-plane position were kept identical to those used for the Au-supported nanoarray. A uniform mesh size of 0.5 nm was employed throughout the entire simulation domain to accurately resolve the nanoscale Au structures and the strongly localized electromagnetic fields within the gap regions.

Frequency-domain power monitors were placed above and below the structure to obtain the reflection (R) and transmission (T) spectra, respectively. The absorptance was subsequently calculated as:

$$A = 1 - R - T$$

The local electromagnetic field enhancement was characterized by [30,31]:

$$\frac{|E|^2}{|E_0|^2}$$

where E is the local electric field amplitude and E_0 is the incident electric field amplitude. Electric field distributions were further extracted in three representative planes: the central x-z plane passing through the truncated pyramid, an upper x-y plane located 2 nm above the pyramid top surface, and a gap x-y plane located 5 nm above the pyramid bottom. These field distributions were used to identify the spatial localization of the plasmonic hotspots, particularly within the nanoscale gaps between neighboring Au nanostructures.

To estimate the electromagnetic contribution to SERS, the electromagnetic enhancement was expressed as the product of the local electric field intensity enhancements at the excitation and Raman-scattered wavelengths:

$$G_{em}(r) \approx F(r, \lambda_{ex}c) \times F(r, \lambda_r)$$

where $\lambda_{ex}c$ and λ_r denote the excitation and Raman-scattered wavelengths, respectively, and $F(r,\lambda) = |E(r,\lambda)|^2/|E_0|^2$ is the local electric field intensity enhancement at position r and wavelength λ. When the local field enhancements at the excitation and Raman-scattered wavelengths are assumed to be approximately equal, the expression reduces to the commonly used $|E|^4$ approximation:

$$G_{em}(r) \approx |F(r, \lambda_{ex}c)|^2 = |F(r, \lambda_{ex}c)|^2/|E_0|^2$$

4. Conclusions

A cross-wavelength hierarchical metasurface sensor integrating THz sensing and SERS enhancement was numerically investigated. The proposed CHMS exhibits four THz resonances, among which the 1.70 THz mode shows the strongest refractive-index response with a sensitivity of 133.4 GHz/RIU. In the optical regime, strong localized near-field enhancement is generated within the nanoscale gaps of the truncated-pyramidal Au nanoarray, with the dominant enhancement occurring near 621.2 nm. The SERS nanoarray introduces only a limited perturbation to the THz response, whereas the underlying CHMS structure noticeably modifies the optical near-field characteristics. In the optical regime, the local supporting environment influences the near-field characteristics of the Au nanoarray, while the additional bare Au control indicates that the pronounced localized enhancement is

primarily associated with the nanostructures and their nanogap coupling rather than the flat Au-supporting layer alone. Dimensional and positional-deviation analyses further show that the THz resonance frequencies remain relatively stable within the investigated ranges, while the resonance depths and SERS near-field response are more sensitive to structural misalignment. The substantial variations in THz resonance depth may affect resonance visibility and the reliability of practical refractive-index sensing, highlighting the importance of accurate interlayer alignment. These results provide useful guidance for the design and fabrication of integrated cross-wavelength THz–SERS metasurfaces.

Supplementary Materials: The following supporting information can be downloaded at https://www.mdpi.com/article/10.3390/molecules31234336/s1, Figure S1: Electric field distributions at 0.50, 1.18, 1.36, and 1.70 THz; Figure S2: Surface current distributions at 0.50, 1.18, 1.36, and 1.70 THz; Figure S3: Comparison of the localized electric field distributions at 621 and 633 nm; Figure S4: Gap-plane electric field distributions at representative Raman excitation wavelengths; Figure S5: Comparison of the maximum electric field intensity enhancement spectra for the bare Au-supporting layer and the Au-supported nanoarray; Table S1: Raw data for THz interlayer positional deviations; Table S2: Raw data for SERS nanostructure positional deviations; Table S3: Mesh-refinement sensitivity of the local electric field intensity enhancement.

Author Contributions: Conceptualization, M.G. and Y.C.; methodology, M.G.; software, Y.C.; validation, M.G. and Y.C.; formal analysis, M.G.; investigation, Y.C.; resources, M.G.; data curation, Y.C.; writing—original draft preparation, M.G.; writing—review and editing, Y.C.; visualization, Y.C.; supervision, M.G.; project administration, M.G.; funding acquisition, M.G. All authors have read and agreed to the published version of the manuscript.

Funding: This research was funded by the Yinfeng Program of Tangdu Hospital, Fourth Military Medical University (No. 2025YFJH002).

Institutional Review Board Statement: Not applicable.

Informed Consent Statement: Not applicable.

Data Availability Statement: The original contributions presented in this study are included in the article and Supplementary Materials. Further inquiries can be directed to the corresponding author.

Conflicts of Interest: The authors declare no conflicts of interest.

References

1. Haddad, J.; Bousquent, B.; Canioni, L.; Mounaix, P. Review in terahertz spectral analysis. *TrAC Trends Anal. Chem.* **2013**, *44*, 98–105. [CrossRef]
2. Kumamoto, Y.; Harada, Y.; Takamatsu, T.; Tanaka, H. Label-free molecular imaging and analysis by Raman spectroscopy. *Acta Histochem. Cytochem.* **2018**, *51*, 101–110. [CrossRef] [PubMed]
3. Banks, P.; Kleist, E.; Ruggiero, M. Investigating the function and design of molecular materials through terahertz vibrational spectroscopy. *Nat. Rev. Chem.* **2023**, *7*, 480–495. [CrossRef] [PubMed]
4. Chen, J.; Ding, W.; Luo, Z.; Loo, B.; Yao, J. Probing single molecules and molecular aggregates: Raman spectroscopic advances. *J. Raman Spectrosc.* **2016**, *47*, 623–635. [CrossRef]
5. Zhang, S.; Qi, Y.; Tan, S.; Bi, R.; Olivo, M. Molecular Fingerprint Detection Using Raman and Infrared Spectroscopy Technologies for Cancer Detection: A Progress Review. *Biosensors* **2023**, *13*, 557. [CrossRef] [PubMed]
6. Wang, Y.; Bai, B.; Ma, C.; Zhang, Q.; Huang, H.; Luo, X.; Liu, X.; Ying, Y.; Xie, L. Cross-Wavelength Hierarchical Metamaterials Enabled for Trans-Scale Molecules Detection Simultaneously. *Adv. Sci.* **2022**, *9*, 2105447. [CrossRef] [PubMed]
7. Jin, W.; Ran, J.; Liang, L.; Tian, H.; Dou, X.; Xie, F.; Chapelle, M.; Fu, W.; Yang, X. A THz/SERS dual-mode immunoassay based on gold nanoparticle coupled metasurfaces for sensitive detection of tumor markers. *ACS Appl. Nano Mater.* **2026**, *9*, 3877–3888. [CrossRef]
8. Zhang, Z.; Zhao, R.; Cong, M.; Qiu, J. Developments of terahertz metasurface biosensors: A literature review. *Nanotechnol. Rev.* **2024**, *13*, 20230182. [CrossRef]
9. Liu, B.; Peng, Y.; Jin, Z.; Wu, X.; Gu, H.; Wei, D.; Zhu, Y.; Zhuang, S. Terahertz ultrasensitive biosensor based on wide-area and intense light-matter interaction supported by QBIC. *Chem. Eng. J.* **2023**, *462*, 142347. [CrossRef]

10. Sun, H.; Cao, Y.; Li, L.; Ma, L.; Chen, Y.; Jin, S.; Liang, S.; Xu, P.; Wu, W. A high-efficiency terahertz sensor based on surface lattice resonance metasurface for biochemical detection. *Sens. Actuators A Phys.* **2024**, *377*, 115711. [CrossRef]
11. Kneipp, J.; Kneipp, K. Surface enhanced nonlinear Raman processes for advanced vibrational probing. *ACS Nano* **2024**, *18*, 20851–20860. [CrossRef] [PubMed]
12. Ma, L.; Zhou, R.; Yang, X.; Dai, Z.; Xu, Q.; Zhang, Y.; Wang, C.; Guo, Z.; Ye, Y.; Zou, X.; et al. Cross-wavelength Hierarchical Metamaterials-Enabled SERS-Terahertz Dual-Modal Sensor for Multipesticide Detection. *Anal. Chem.* **2025**, *97*, 21324–21332. [CrossRef] [PubMed]
13. Zhang, Y.; Yao, Y.; Guang, Z.; Xue, J.; Wang, Q.; Gong, Q.; Ali, Z.; Yang, Z. A High-Sensitivity Fiber Biosensor Based on PVDF-Excited Surface Plasmon Resonance in the Terahertz Band. *Photonics* **2023**, *10*, 1159. [CrossRef]
14. Xue, J.; Zhang, Y.; Guang, Z.; Hu, J.; Zhao, F.; Liu, Y.; Shao, L. MoS 2 surface plasmon resonance based high-resolution THz biosensor using a dual D-shaped channel micro-structured fiber. *Opt. Laser Technol.* **2025**, *180*, 111387. [CrossRef]
15. Agarwal, P.; Kishor, K.; Sinha, R.K. All Dielectric High Q-Factor Metasurface Refractive Index Sensor Based on Dual Fano Resonances in THz Region. *IEEE Sens. Lett.* **2024**, *8*, 3500704. [CrossRef]
16. Lu, X.; Ge, H.; Jiang, Y.; Zhang, Y. Design and analysis of a dual-band THz metamaterial sensor with high refractive index sensitivity. *Front. Phys.* **2022**, *10*, 973033. [CrossRef]
17. Liang, Y.; Zhao, Q.; Lv, Y.; Lu, R.; Ling, J.; Mo, H.; Ma, M.; Zhang, Y.; Mo, K. Highly sensitive and polarization-insensitive terahertz microfluidic biosensor based on gap plasmon model. *Results Phys.* **2023**, *51*, 106693. [CrossRef]
18. Xu, Y.; Aljuhani, W.; Zhang, Y.; Ye, Z.; Li, C.; Bell, S.E.J. A practical approach to quantitative analytical surface-enhanced Raman spectroscopy. *Chem. Soc. Rev.* **2025**, *54*, 62–84. [CrossRef] [PubMed]
19. Shin, H.-J.; Yoo, J.; Park, E.; Song, E.H.; Nam, J.-M. Plasmonic Nanogap Probes for Surface-Enhanced Raman Scattering-Based Bioimaging and Analysis. *J. Phys. Chem. C* **2024**, *128*, 17815–17824. [CrossRef]
20. Hardy, M.; Goldberg Oppenheimer, P. 'When is a hotspot a good nanospot'—Review of analytical and hotspot-dominated surface enhanced Raman spectroscopy nanoplatforms. *Nanoscale* **2024**, *16*, 3293–3323. [CrossRef] [PubMed]
21. Feng, G.; Chen, Z.; Mi, X.; Sun, F.; Yang, Y.; Wang, Y.; Chen, S. All-dielectric terahertz metasurfaces with high Q Fano resonance based on indirect perturbation and bound states in the continuum. *Opt. Laser Technol.* **2023**, *164*, 109578. [CrossRef]
22. Luo, S.; Mancini, A.; Wang, F.; Liu, J.; Maier, S.A.; de Mello, J.C. High-Throughput Fabrication of Triangular Nanogap Arrays for Surface-Enhanced Raman Spectroscopy. *ACS Nano* **2022**, *16*, 7438–7447. [CrossRef] [PubMed]
23. Li, K.; Tang, X.; Wang, H.; Huang, M.; Liu, G.; Zhou, Y.; Huang, W.; Zuo, Z.; Lu, Y. Large-area opposing double nanocrescents-nanoparticle arrays for polarization dependent SERS effects. *Appl. Surf. Sci.* **2023**, *613*, 156117. [CrossRef]
24. Singh, S.; Singh, S. Sectoral-resonator dual-band metamaterial absorber with wide-incidence response for THz biosensing. *Phys. B* **2026**, *739*, 418928. [CrossRef]
25. Wollack, E.J.; Cataldo, G.; Miller, K.H.; Quijada, M.A. Infrared properties of high-purity silicon. *Opt. Lett.* **2020**, *45*, 4935–4938. [CrossRef] [PubMed]
26. Jain, P.; Chhabra, H.; Chauhan, U.; Prakash, K.; Gupta, A.; Soliman, M.; Islam, M.; Islam, M. Machine learning assisted hepta band THz metamaterial absorber for biomedical applications. *Sci. Rep.* **2023**, *13*, 1792. [CrossRef] [PubMed]
27. Ma, A.; Zhong, R.; Wu, Z.; Wang, Y.; Yang, L.; Liang, Z.; Fang, Z.; Liu, S. Ultrasensitive THz sensor based on centrosymmetric F-shaped metamaterial resonators. *Front. Phys.* **2020**, *8*, 584639. [CrossRef]
28. Zeng, Z.; Liu, Y.; Wei, J. Recent advances in surface-enhanced Raman spectroscopy (SERS): Finite-difference time-domain (FDTD) method for SERS and sensing applications. *TrAC Trends Anal. Chem.* **2016**, *75*, 162–173. [CrossRef]
29. Johnson, P.; Christy, R. Optical constants of the noble metals. *Phys. Rev. B* **1972**, *6*, 4370–4379. [CrossRef]
30. Ding, S.; You, E.; Tian, Z.; Moskovits, M. Electromagnetic theories of surface-enhanced Raman spectroscopy. *Chem. Soc. Rev.* **2017**, *46*, 4042–4076. [CrossRef]
31. Le Ru, E.; Etchegoin, P. Rigorous justification of the $|E|^4$enhancement factor in Surface Enhanced Raman Spectroscopy. *Chem. Phys. Lett.* **2006**, *423*, 63–66. [CrossRef]

Disclaimer/Publisher's Note: The statements, opinions and data contained in all publications are solely those of the individual author(s) and contributor(s) and not of MDPI and/or the editor(s). MDPI and/or the editor(s) disclaim responsibility for any injury to people or property resulting from any ideas, methods, instructions or products referred to in the content.